RSC Advances

PAPER

View Article Online
View Journal | View Issue

Cite this: *RSC Adv.*, 2018, **8**, 39187

Fabrication of novel AgBr/$Bi_{24}O_{31}Br_{10}$ composites with excellent photocatalytic performance

Zuming He,[ab] Yongmei Xia*[c] and Jiangbin Su[ab]

Received 22nd October 2018
Accepted 15th November 2018

DOI: 10.1039/c8ra08733d

rsc.li/rsc-advances

Novel porous AgBr/$Bi_{24}O_{31}Br_{10}$ (AB/BOB) heterojunction composites were prepared by a hydrothermal calcination-ion exchange route and their physico-chemical properties were characterized by XRD, XPS, SEM, EDX, UV-vis DRS, BET and electrochemical measurements. The photocatalytic activity of the composites consisting of different AB/BOB mass ratios was evaluated by degradation of methylene blue (MB) under visible light irradiation. Compared with pure AB and BOB, the porous 20% AB/BOB composite exhibits much enhanced photocatalytic activity with good cycling stability. The significant enhancement in photoactivity is contributed to by both a high adsorption capacity and the separation efficiency of photo-generated electron–hole (e^-–h^+) pairs *via* a *Z*-scheme mechanism. In addition, radical scavenging experiments confirm that the reactive ·OH radicals play an important role in the photocatalytic reaction. The novel (AB/BOB) heterojunction composites could have a promising application in treatment of various dyestuff wastewaters on a large scale.

1. Introduction

Semiconductor photocatalysis is an important technology that utilizes light to degrade organic pollutants in wastewater.[1,2] Over the past decade, TiO_2 and ZnO have received tremendous attention owing to their advantages of nontoxic nature, low cost, high photosensitivity, and eco-friendly features in the field of photocatalytic applications.[3,4] Unfortunately, the wide band gap photocatalysts can only absorb photons in the ultraviolet (UV) range, and thus their photocatalytic activity is limited under irradiation of solar light as it contains only 5% UV light.[5,6] To achieve efficient use of solar energy, it is urgent to explore and develop new types of visible-light-responsive photocatalysts.[7–10]

Recently, $Bi_{24}O_{31}Br_{10}$ (designated as BOB) has attracted substantial attention as a promising photocatalyst due to its unique crystal structure, energy band structure, and excellent stability.[11,12] For example, Shang and coworkers prepared a plate-like BOB photocatalyst by a chemical precipitation method, which displayed good photocatalytic performances for the reduction of Cr(VI) in wastewater.[13] Liu *et al.* used Er doping to enhance the photocatalytic performance of BOB.[14] However, the reported photocatalytic ability of this kind of material is still unsatisfactory. Therefore, further structural modifications are inevitable. To date, many strategies have been developed to improve the photocatalytic performances of photocatalysts, *e.g.*, doping, surface functionalization, noble metal decoration, construction of heterojunction and so on.[15–18] Especially, the construction of heterojunction photocatalysts by coupling two semiconductors with matching band structures could facilitate the migration and separation of photo-generated carries for improving the photocatalytic activity. Very recently, Peng *et al.* Reported fabrication of $Bi_{12}O_{17}Br_2/Bi_{24}O_{31}Br_{10}$ Type II heterostructures by calcining BiOBr/$Bi(OHC_2O_4)\cdot 2H_2O$.[19] Lou's research team reported $Bi_{24}O_{31}Br_{10}$ possessed narrower band gap and higher photocatalytic activity compared with BiOI.[20] Li *et al.* synthesized $Bi_{24}O_{31}Cl_{10}$/BiOCl heterojunctions with enhanced photocatalytic activity *via* a facile solvothermal method.[21] They found that the nanocomposites exhibited superior photocatalytic performances. To the best of our knowledge, porous AgBr/$Bi_{24}O_{31}Br_{10}$ (designated as AB/BOB) heterojunction composites built up by ultrathin nanosheets have not been studied so far.

In this current work, we first designed and fabricated novel porous AB/BOB heterojunction composites *via* a hydrothermal calcination-ion exchange route. The structure, morphology, specific surface and photo-absorption performance of the as-synthesized AB/BOB composites were characterized. The photocatalytic performance of the composites was investigated by the degradation of methylene blue (MB) dye under visible light irradiation and was found to be much higher than that of bare AB and BOB. Moreover, the photocatalytic mechanism of the oxidation of MB was analyzed and discussed in detail according to the experimental results.

[a]*Huaide School, Changzhou University, Jingjiang 214500, China*
[b]*School of Mathematics & Physics, Changzhou University, Changzhou 213164, China*
[c]*School of Materials and Engineering, Jiangsu University of Technology, Changzhou 213001, China. E-mail: xiaweiwei906@126.com*

2. Experimental

2.1. Materials

Bismuth nitrate pentahydrate ($Bi(NO_3)_3 \cdot 5H_2O$) and sodium hydroxide (NaOH) were obtained from Tianjin Kermel Chemical Reagent Co. Ltd. Silver nitrate ($AgNO_3$) and potassium bromide (KBr) were obtained from Jiangsu Qiangsheng Functional Chemical Reagent Co. Ltd. Glucose ($C_6H_{12}O_6 \cdot H_2O$), ethylene glycol (EG) and methylene blue (MB) were purchased from Jiangsu Yong Feng Chemical Reagent Co., Ltd. All the reagents used in this experiment were of analytical grade without further treatment and all the solutions were prepared with deionized water.

2.2. Preparation of porous BOB microspheres

Pure BOB was prepared by a hydrothermal-calcinating method. 1.189 g (0.006 mol) $C_6H_{12}O_6 \cdot H_2O$ was dissolved in 50 mL of EG. Then 4.8507 g (0.01 mol) of $Bi(NO_3)_3 \cdot 5H_2O$ and 0.4958 g (0.0042) KBr were completely dissolved in above solution under magnetic stirring for 30 min to form a clear mixture. The resulting clear mixture was transferred into a 100 mL Teflon-lined autoclave and kept at 160 °C for 12 h. After the reaction, the autoclave was cooled down to room temperature naturally. The product was collected by filtering, washed several times with deionized water and alcohol, and dried in air at 80 °C for 8 h. The BOB powder was further subjected to calcination treatment at 450 °C for 3 h.

2.3. Preparation of AB/BOB heterojunction composites

AB/BOB heterojunction composites were prepared by an ion exchange method. In a typical preparation process, equal moles of NaBr and $AgNO_3$ were separately dissolved in 30 mL of deionized water. A certain amount of as-prepared BOB powder was ultrasonically dispersed into the NaBr solution by stirring for 30 min. The $AgNO_3$ solution was then added dropwise to the BOB and NaBr mixture suspension solution under vigorous stirring. After stirring for 2 h, the resulting product was collected, repeatedly washed several times with distilled water and ethanol, and then dried at 80 °C in air for 10 h. According to this method, the composites with different AgBr weight fractions were prepared. The samples obtained at $m_{AgBr}/(m_{AgBr} + m_{Bi_{24}O_{31}Br_{10}}) = 10\%$, 20% and 25% were designated as 10% AB/BOB, 20% AB/BOB and 25% AB/BOB, respectively.

2.4. Sample characterization

Crystallographic structures of the as-synthesized samples were characterized using X-ray diffractometer (XRD) with Cu K_α radiation (D/max-2500, Rigaku, $\lambda = 1.5406$ Å) in a scanning speed of 5° min^{-1}. The morphology, microstructure, and energy-disperse X-ray (EDX) spectra were taken with an ultra-high resolution field-emission scanning electron microscope (FE-SEM, SUAPR55, Germany Zeiss). The elemental compositions and chemical states of the samples were measured using X-ray photoelectron spectroscopy (XPS, Thermo ESCALAB 250XI, USA). The ultraviolet-visible diffuse reflectance spectra (UV-vis DRS) were obtained using a UV-vis spectrophotometer (UV-2450, Shimadzu, Japan). Electrochemical measurement was conducted with electrochemical analyzer (CHI660C Instruments, Shanghai, China) in a conventional three electrode cell, using an Ag/AgCl electrode as the reference electrode and a Pt plate as the counter electrode. The Brunauer–Emmett–Teller (BET) surface area was measured using a Micrometrics (TriStar II 3020 Mike instruments of America).

2.5. Photocatalytic test

The photocatalytic activity of AgBr, BOB, and AB/BOB composites was assessed by the degradation of MB (20 mg L^{-1}) under the irradiation of a 500 W Xenon lamp with the UV-cut filter ($\lambda >$ 420 nm) and the light intensity of 0.4 mW cm^{-2} was ensured. 100 mg of the photocatalyst was put into 100 mL MB solution and kept in the dark for 20 min. During each photocatalytic experiment, 3 mL of the suspension was withdrawn every 5 minutes and separated to remove the photocatalyst powder. The change of the MB concentration was measured by UV-vis spectrometer. The dye degradation efficiency (D) can be calculated according to eqn (1)

$$D(\%) = [(A_0 - A_t)/A_0] \times 100\% \quad (1)$$

where A_0 and A_t represented the concentration of MB solution at the beginning and at time t.

2.6. Active species trapping experiment

In the photocatalytic reaction, three kinds of active species could be generated, involving holes (h^+), superoxide ($\cdot O_2^-$) and hydroxyl ($\cdot OH$).[22] Their contribution was tested in another MB photodegradation experiment with the separate addition of 1 mmol L^{-1} (mM) ethylenediaminetetraacetic acid disodium salt (EDTA-2Na), 1 mM benzoquinone (BQ) and 1 mM isopropanol (IPA), which acted as scavengers of h^+, $\cdot O_2^-$ and $\cdot OH$, respectively.

2.7. Electrochemical measurements

Electrochemical measurements were performed using a three-electrode system on a CHI660E electrochemical workstation. The reference electrode and counter electrode were Ag/AgCl and platinum wire, respectively. 0.2 mol L^{-1} (M) Na_2SO_4 aqueous solution was used as the electrolyte. The work electrode was prepared according to the procedure as described in the literature.[23] In brief, 20 mg of the sample was dispersed into 100 μL of 25% professional video assistant (PVA) solution under ultrasonication for 1 h to form suspension. The suspension was then dropped onto a 1 cm × 2 cm fluorine-doped tin oxide (FTO) slice (FTO substrate was cleaned) with an effective working area of 1 cm^2, followed by drying at 80 °C for 5 h. A 300 W Xe arc lamp equipped with a cut-off filter ($\lambda > 420$ nm, the light intensity is 0.4 mW cm^{-2}) was utilized as the light source.

3. Results and discussion

3.1. XRD analysis

The crystal structures of the as-synthesized samples were characterized by XRD technology. As can be seen from Fig. 1, the diffraction peaks of BOB sample can be well indexed to the monoclinic BOB phase (PDF#75-0888). Several strong peaks and the corresponding crystal planes are observed at 10.52° (102), 25.05° (206), 29.76° (213), 31.82° (117), 46.03° (201) and 57.02° (011).[24] For pure AgBr, the major diffraction peaks with 2θ = 26.71°, 30.94°, 44.32°, 55.03°, 64.48° and 73.23° can be indexed to the (111), (200), (220), (222), (400) and (420) crystal facets of the cubic AgBr phase (PDF#79-0149), respectively.[25] As for the patterns of the AB/BOB composites, all the peaks can be accurately indexed to the cubic AgBr phase and monoclinic BOB phase, where no other impurity peaks are observed. In addition, the intensities of AgBr diffraction peaks increase gradually with the increase of the mass fraction of AgBr.

3.2. XPS analysis

The chemical states of elements for the 20% AB/BOB nanocomposite were determined by XPS measurement, and the results are shown in Fig. 2. Five elements including Br, Ag, Bi, C and O are detected in the XPS survey spectrum (Fig. 2(a)), from which the obtained atomic proportion of Ag, Bi and Br is every close to that of stoichiometric composition of the sample. The C 1s XPS spectrum as given in Fig. 2(b) shows two peaks at 284.84 and 287.56 eV, which might be assigned to the adventitious hydrocarbon from the XPS instrument itself used to calibrate the binding energy scale. Fig. 2(c) depicts two strong peaks at 368.2 and 374.3 eV in the AgBr and 20% AB/BOB nanocomposite which can be attributed to Ag $3d_{5/2}$ and Ag $3d_{3/2}$, respectively.[26] This implies that silver species is in the form of Ag^{+} oxidation state. The existence of Ag metal state can be ruled out since no additional peak is visible in the Ag 3d XPS spectrum. As seen from the Bi 4f XPS spectrum of the BOB and 20% AB/BOB nanocomposite are shown in Fig. 2(d), the peaks located at 159.1 and 164.41 eV are ascribed to Bi $4f_{7/2}$ and Bi $4f_{5/2}$, respectively, indicating that Bi species exhibits +3 oxidation state in the 20% AB/BOB nanocomposite.[27] Fig. 2(e) displays the Br 3d spectrum of the AgBr and 20% AB/BOB nanocomposite, in which the two typical peaks located at binding energies of 69.2 and 68.4 eV are due to Br $3d_{3/2}$ and Br $3d_{5/2}$ peaks, respectively, indicating that the Br element is mainly in the form of Br^{-} in the composite.[28,29] As clearly illustrated in Fig. 2(f), the O 1s XPS spectrum of the BOB and 20% AB/BOB nanocomposite can be fitted into three peaks separately located at 529.87, 530.89 and 531.82 eV. The signal peak at 529.87 eV is attributed to layer-structured Bi–O bonds. The peaks at 531.89 and 531.82 eV can be assigned to the O–H and C–OH, respectively.[30,31]

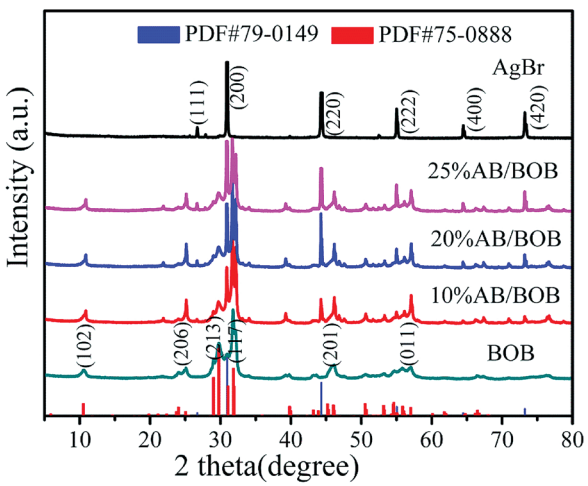

Fig. 1 XRD patterns of pure AgBr, BOB and AB/BOB nanocomposites.

3.3. SEM and EDX analysis

In order to investigate the typical morphology and detailed structure of the as-prepared samples, FE-SEM images of pure AgBr, pure BOB and 20% AB/BOB nanocomposite were acquired and illustrated in Fig. 3. The pristine AgBr exhibits a morphology of smooth spherical-like particles with the average size of 500–800 nm (Fig. 3(a)). It can be observed from Fig. 3(b) that the pure BOB presents dispersed 3D flower-like porous microspheres, which are composed of nanosheets. The thickness of the nanosheets is about 30 nm according to the high-magnification SEM image inserted in Fig. 3(b). From Fig. 3(c), it is seen that AgBr particles are coupled with BOB nanosheets to form AB/BOB heterojunction nanocomposites. The chemical composition of the 20% AB/BOB composite is further confirmed by the EDX spectrum, as shown in Fig. 3(d). It is noted that EDX is sensitive to heavy elements like Ag and Bi, but not to light elements like C and O.[31] This means that the content of heavy elements can be precisely determined from EDX. It can be found that the only detectable elements are O, Ag, Bi and Br (C and Pt come from the conductive tape). The atom ratio of Ag and Bi is obtained as 1 : 3, which is in good agreement with the Ag/Bi atomic ratio of the 20% AB/BOB nanocomposite.

3.4. Optical property analysis

To acquire the insights into the optical properties of the samples, their UV-vis DRS spectra were measured and are presented in Fig. 4(a). The pure AgBr exhibits the main absorption in the wavelength region ranging from 200 to 475 nm. The band gap energies (E_g) of the samples can be obtained based on the equation $\alpha h\nu = A\ (h\nu - E_g)^{1/2}$,[32,33] where α, h, ν, E_g and A are absorption coefficient, Planck constant, light frequency, band gap and transition constant, respectively. As seen from Fig. 4(b), the derived band gap of AgBr and BOB are about 2.6 and 2.8 eV, respectively.

3.5. BET analysis

The nitrogen adsorption–desorption isotherm was used to investigate the BET specific surface area and porous structure of the BOB and AB/BOB composite, as shown in Fig. 5(a). The BET surface areas of BOB, 10% AB/BOB, 20% AB/BOB and 25% AB/BOB composite were estimated to be 68.58 $cm^2\ g^{-1}$, 70.61 cm^2

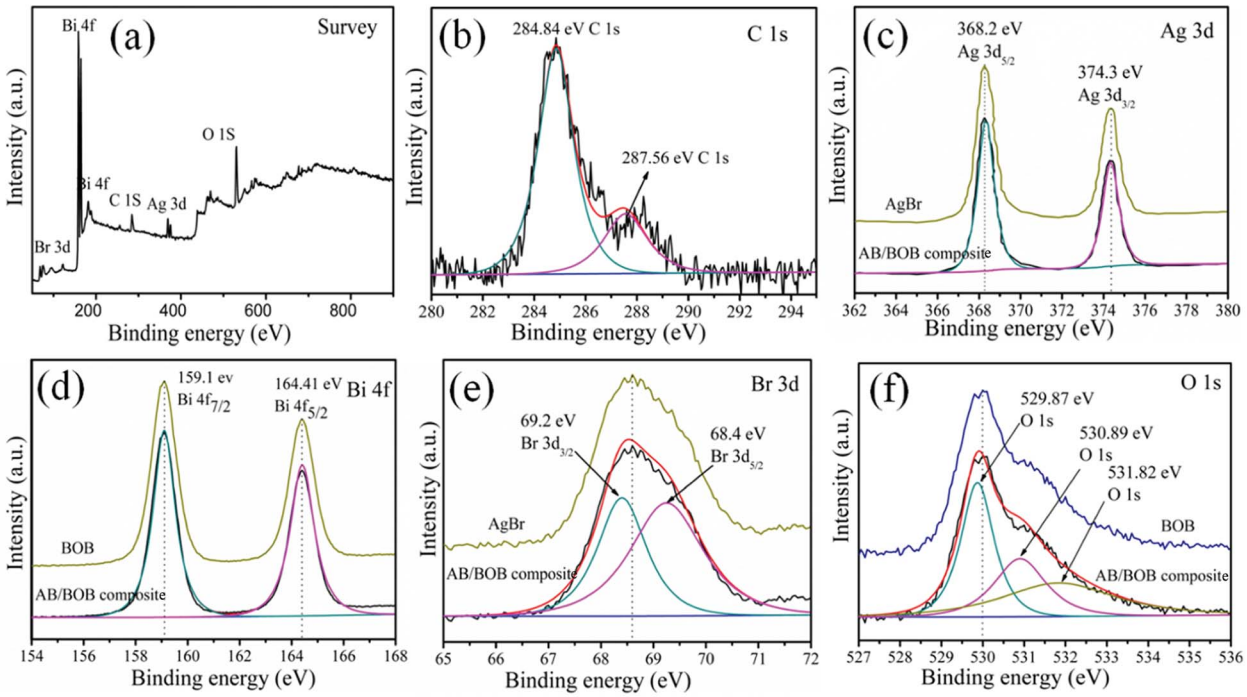

Fig. 2 XPS spectra of the 20% AB/BOB nanocomposite, (a) survey, (b) C 1s, (c) Ag 3d, (d) Bi 4f, (e) Br 3d and (f) O 1s.

g^{-1}, 75.29 cm^2 g^{-1}, and 72.81 cm^2 g^{-1}, respectively. In comparison to pure BOB, the BET surface areas of AB/BOB composites showed a slight increase, which could be ascribed to the decoration of AgBr nanoparticles on the surface of BOB. But when excessive introduction of AgBr cover (or blocking) the porous structure around of BOB nanosheet. Therefore, the

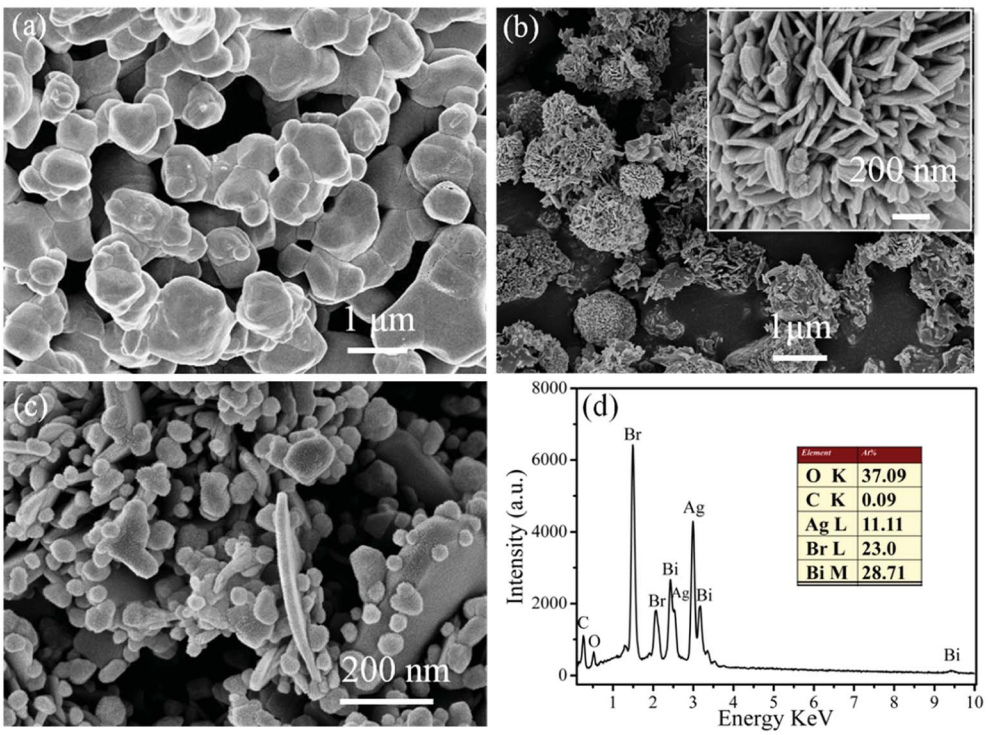

Fig. 3 (a)–(c) SEM images of AgBr, BOB and 20% AB/BOB, respectively. The inset in (b) shows the high-magnification SEM image of 20% AB/BOB. (d) EDX pattern of 20% AB/BOB nanocomposite.

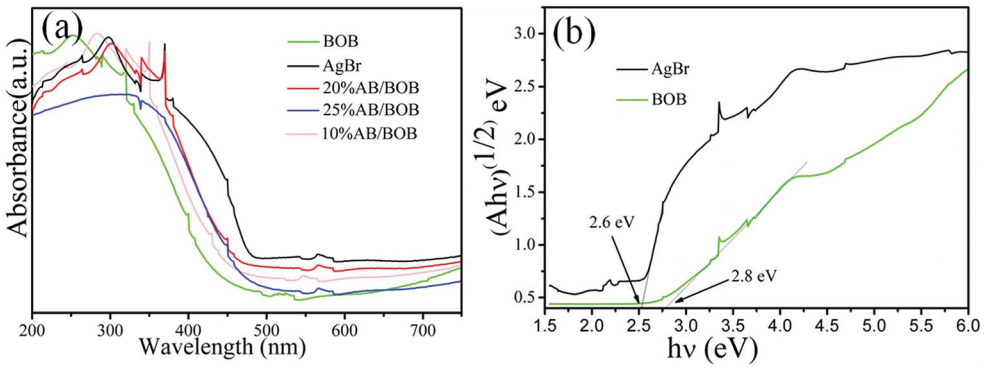

Fig. 4 UV-vis DRS spectra (a) and $(\alpha h\nu)^{1/2}$ *versus* $h\nu$ (b) of the as-prepared samples.

surface area of the composites decreased as the introduction of AgBr to BOB. As a result, significant enhancements in degradation efficiency would be ultimately achieved. According to the IUPAC classification, a type IV the isotherm with a narrow hysteresis loop at high relative pressures can be found, indicating the presence of porous structure of the composite.[34] As illustrated in Fig. 5(b), the 20% AB/BOB composite exhibits a narrow pore-size distribution with average pore diameter around 12.59 nm. Table 1 summarizes the BET specific surface area, pore volume and pore diameter of AgBr, BOB, 10% AB/BOB, 20% AB/BOB and 25% AB/BOB composites. Among these samples, the 20% AB/BOB composite has the largest BET specific surface area and porous volume, and the smallest pore diameter, implying that the 20% AB/BOB composite can provide more active sites and adsorb more reactive species.

3.6. Photocatalytic properties

In order to investigate the adsorbability of MB on the samples, we carried out the adsorption experiments in the dark, as shown in Fig. 6(a). It is can be seen that the adsorption process proceeds very fast, and it takes about 20 min to reach adsorption–desorption equilibration for the samples. All the samples display a strong adsorbability toward MB; particularly, the 20% AB/BOB composite exhibits the highest adsorbability and the adsorption percentage of the dye reaches 42.1% after 20 min. The photocatalytic activities of the products were assessed by the degradation of MB solutions under exposure to visible light and the results are plotted in Fig. 6(a). It is seen that the direct photolysis of MB without photocatalyst can almost be neglected, indicating that MB exhibits a good stability under visible light irradiation. The as-prepared BOB shows moderate catalytic activity, and only 16.1% MB degradation is achieved after 20 min irradiation. The pure AgBr shows better photocatalytic activity than pure BOB and about 27% MB is degraded under visible light irradiation for 20 min. It is observed that under visible light irradiation, with the increase of AgBr content, the photocatalytic activity of AB/BOB composites first increases and then declines. All AB/BOB composites photocatalysts exhibit enhanced photocatalytic activity compared to pure AgBr and BOB, indicating that the coupling of BOB with AgBr can effectively improve the photocatalytic activity. The 20% AB/BOB composite exhibits the highest photocatalytic activity, and the photocatalytic degradation percentage of MB reaches 98.7% after 20 min. It is generally accepted that an appropriate ratio of two semiconductors is required to achieve the most heterostructures, and thus the photogenerated electron/hole pairs can be efficiently separated due to the interfacial charge transfer.[35,36] This is the main reason that the 20% AB/BOB composite manifests the highest photocatalytic activity among the AB/

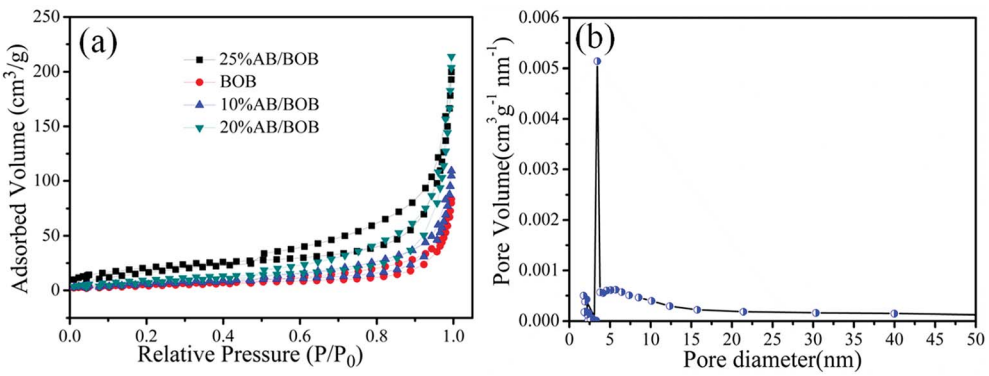

Fig. 5 Nitrogen adsorption–desorption isotherm of the samples (a) and the corresponding pore-size distribution of the 20% AB/BOB composite (b).

Table 1 Surface area, pore volume and pore diameter of the as-prepared samples

Samples	porous volume ($cm^3\ g^{-1}$)	BET ($cm^2\ g^{-1}$)	Pore diameter (nm)
AgBr	0.009	39.80	30.25
BOB	0.015	68.58	25.41
10% AB/BOB	0.018	70.61	15.35
20% AB/BOB	0.018	75.29	12.59
25% AB/BOB	0.017	72.81	16.21

BOB composites. Fig. 6(b) demonstrates the plots of $-\ln(C_t/C_0)$ *versus* irradiation time (t) for the dye degradation over the samples. The first-order kinetic equation $-\ln(C_t/C_0) = kt$ can be well used to model the photocatalytic removal of RhB, where k, C_0 and C_t, are representative of rate constant, the initial concentration and the concentration at time t, respectively.[37,38] The k values obtained for AgBr, BOB, 10% AB/BOB, 20% AB/BOB and 25% AB/BOB are 0.0565, 0.0767, 0.1122, 0.1883 and 0.127 min^{-1}, respectively. It is noted that the 20% AB/BOB composite exhibits the largest kinetic constant (0.1883 min^{-1}), which is nearly 2.45 times higher than that of pure BOB (0.0767 min^{-1}). This implies that the photocatalytic activity of 20% AB/BOB is about 2.45 times higher than that of bare BOB, which is contributed to the efficient separation of photogenerated electron–hole (e^-–h^+) pairs.

The 20% AB/BOB composite was further investigated by recycling experiments for the photo-degradation of MB in order to explore its stability in dark and under visible light irradiation, as shown in Fig. 7(a). It is seen that although the adsorbability decreases slightly from 42.1% to 38.5% over five consecutive cycles, the photodegradation rate undergoes almost no change, indicating that the composite exhibits high photostability during the process of photocatalysis. In addition, the used 20% AB/BOB was collected and examined by XRD. As seen from Fig. 7(b), the composite after five times of photocatalytic recycling tests exhibits an XRD pattern similar to that of the composite before photocatalytically used, and all the peaks are attributed to cubic phase AgBr and monoclinic-phase BOB. These results demonstrate that 20% AB/BOB has good photocorrosion resistance and excellent stability.

3.7. Photocatalytic mechanism of AB/BOB composites

In order to help understand the photo-generated carrier transfer in AB/BOB composites, we carried out the photoelectrochemical experiments under visible light illumination, which may directly reflect the separation of photo-generated carriers. Fig. 8 displays the photocurrent intensity–time curves of BOB and 20% AB/BOB photoelectrodes over five on-off cycles under visible light irradiation. The result reveals that the 20% AB/BOB composite has a photocurrent density about 5.8 times higher than that of bare BOB under identical conditions. The enhanced photocurrent response of the composite indicates higher separation efficiency of the photo-generated e^-–h^+ pairs.

In the photocatalytic process, the active species responsible for the dye degradation mainly include h^+, $\cdot OH$ and $\cdot O_2^-$. To reveal the roles of the primary active species in the photocatalysis, radical trapping experiments were carried out by adding EDTA-2Na, BQ and IPA into the reaction solution. It is known that EDTA-2Na, BQ and IPA can be used as the good scavengers of h^+, $\cdot O_2^-$ and $\cdot OH$, respectively.[39] Fig. 9 displays the relationship of different scavengers and the photodegradation rate of MB solution in the presence of 20% AB/BOB photocatalyst. It can be found that the addition of EDTA-2Na or BQ does not cause significant deactivation of 20% AB/BOB photocatalyst, and the dye degradation percentage only decreases from 98.7% to 97.7% or 96.7% after 20 min of photocatalytic reaction, indicating that h^+ and $\cdot O_2^-$ play almost no role in the photocatalysis. However, when IPA is added into the reaction solution, the dye degradation is significantly inhibited, revealing that $\cdot OH$ plays an important role in the photocatalytic reaction.

To further understand the photocatalytic mechanism of AB/BOB composites, it is necessary to obtain the conduction band (CB) and the valance band (VB) edge potentials of AgBr and BOB because the redox ability of photo-generated e^- and h^+ are completely dependent on the energy-band potentials of the photocatalysts. The band edge positions of BOB and AgBr can be calculated using the following empirical formula[40]

$$E_{VB} = \kappa - E_0 + 0.5E_g \quad (2)$$

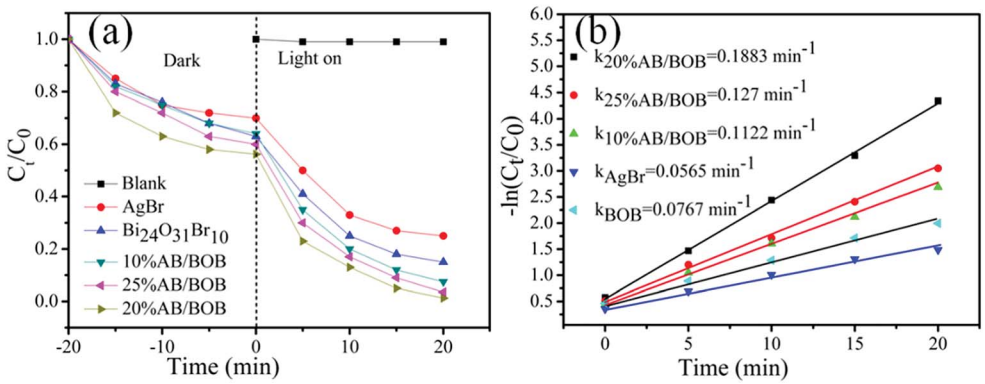

Fig. 6 Time-dependent photodegradation of MB (a) and kinetic curves of the dye degradation (b) over the as-prepared samples under visible light irradiation.

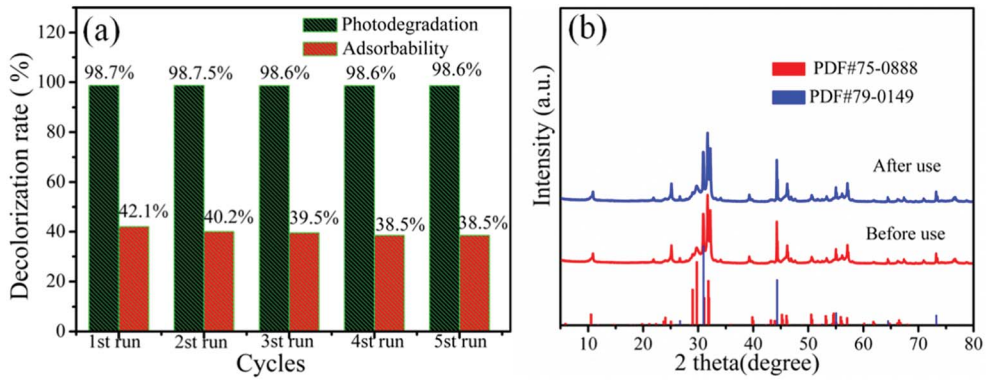

Fig. 7 (a) Cycling degradation efficiency of MB over 20% AB/BOB (reaction for 20 min). (b) XRD patterns of 20% AB/BOB before and after recycling experiment.

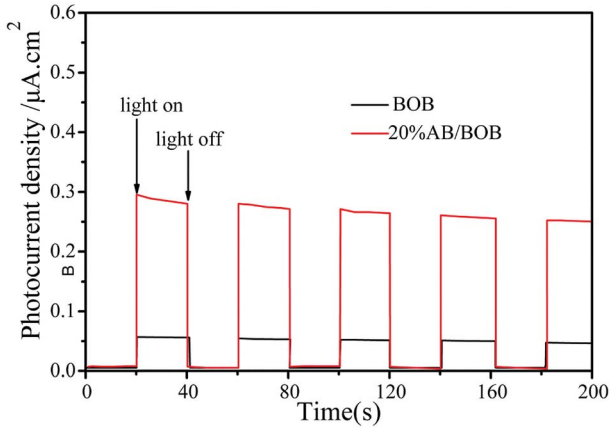

Fig. 8 Photocurrent responses of BOB and 20% AB/BOB composite under visible light irradiation.

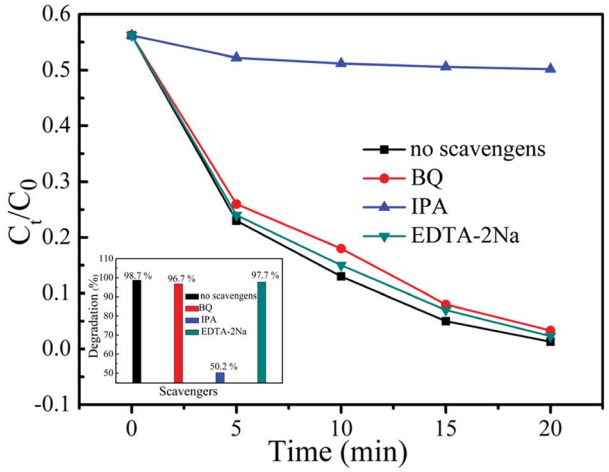

Fig. 9 Effect of IPA, BQ and EDTA-2Na on the MB degradation over 20% AB/BOB composite.

$$E_{CB} = E_{VB} - E_g \quad (3)$$

where E_{VB} and E_{CB} are the VB edge potential and CB edge potential, respectively; κ, E_g and E_0 are the absolute electronegativity, the band gap energy of the semiconductors and the potential energy of a free electrons in a standard hydrogen electrode (4.5 eV), respectively.[41] Based on the measured band gaps of BOB (2.8 eV) and AgBr (2.6 eV), the values of E_{CB} and E_{VB} for BOB are calculated to be 0.13 and 2.93 eV, and those for AgBr are −0.02 and 2.58 eV, respectively, which is consistent with the previous result,[42,43] as presented in Fig. 10(a). It is well known that $\cdot O_2^-$ can be formed through the reaction of oxygen molecules with photogenerated electrons, if the electron potential is more negative than the standard redox potential of $O_2/\cdot O_2^-$(−0.33 eV *vs.* NHE).[44] In this case, the CB potentials of BOB (0.13 eV *vs.* NHE) and AgBr (−0.02 eV *vs.* NHE) cannot make the reaction between photo-generated electrons and O_2 to generate $\cdot O_2^-$.[45] Thus, according to previous work,[46–49] a plausible *Z*-scheme mechanism can be used to explain the charge behaviors of AB/BOB composites in the process of the dye degradation, as shown in Fig. 10(b). Under visible light irradiation with photon energy less than 2.95 eV ($\lambda > 420$ nm), some e^- in the VB of AgBr and BOB could be excited up to a higher potential edge −0.37 and −0.03 V, respectively.[20,50] The reformed CB edge potential of AgBr (−0.37 eV) is more negative than the standard redox potential of $O_2/\cdot O_2^-$(−0.33 eV *vs.* NHE).[51] As a result, the photogenerated e^- can react with O_2 to form $\cdot O_2^-$, then, $\cdot O_2^-$ further reacts with H^+ to produce ·OH. In the meanwhile, the excited electron in the CB of BOB will combine with the photogenerated hole of AgBr. Moreover, the redox potential of $H_2O/\cdot OH$ (+2.72 eV *vs.* NHE[52]) is more negative than the VB potential of BOB (2.93 eV), which implies that the water molecules can be directly oxidized by photo-generated h^+ to form ·OH radicals. By this manner, the photo-generated e^- and h^+ are effectively separated and the recombination of photo-generated e^-–h^+ pairs is heavily inhibited in the AB/BOB composites. Thus it brings out significant enhancement in the photocatalytic activity of the AB/BOB composites for the degradation of organic pollutants.

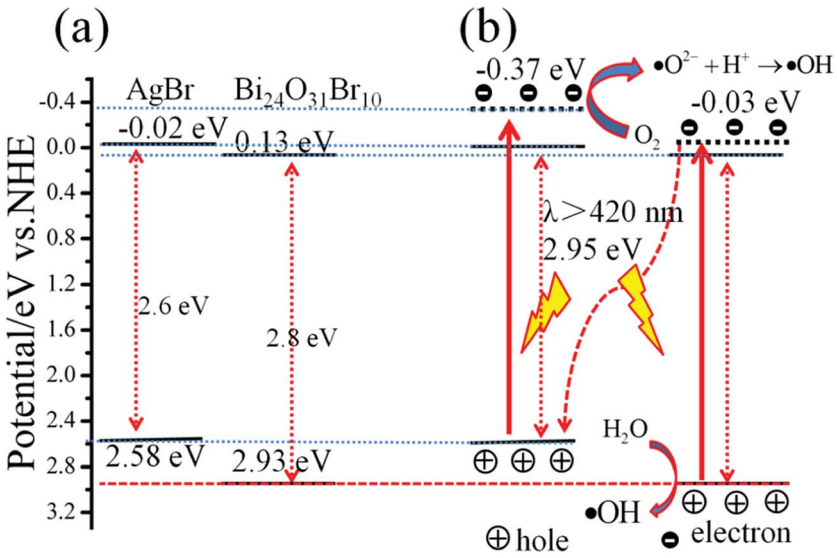

Fig. 10 Schematic band diagram and possible photocatalytic process of AB/BOB composites.

4. Conclusion

In summary, novel AB/BOB *Z*-scheme photocatalysts were triumphantly constructed *via* a hydrothermal calcination-ion exchange route. The as-prepared AB/BOB composites manifest not only superior adsorption performance, but also outstanding photocatalytic ability for the degradation of MB. The significant enhancement of photocatalytic performance for AB/BOB composites can be ascribed to their high BET surface area, ultrathin sheets geometry and high separation efficiency of photo-generated e^-–h^+ pairs *via* a *Z*-scheme mechanism. In addition, the trapping experiments of the active species confirm that ·OH is the main radical species for photocatalytic degradation of MB organic dye molecules under the visible light irradiation. The as-synthesized AB/BOB composites shows a high stability and recyclability, indicating its potential for practical applications.

Conflicts of interest

The authors declare that they have no conflict of interest.

Acknowledgements

This work was supported by the Specialized Research Fund for the Doctoral Program of Jiangsu University of Technology (KYY17011) and the Natural Science Foundation of Jiangsu Province (BK20181043) and the Cooperation Projects between Universities and Enterprises (KYH17020002)

References

1 X. Xu, C. Randorn, P. Efstathiou and J. T. Irvine, A red metallic oxide photocatalyst, *Nat. Mater.*, 2012, **11**, 595–598.
2 M. L. Marin, L. Santos-Juanes, A. Arques, A. M. Amat and M. A. Miranda, Organic photocatalysts for the oxidation of pollutants and model compounds, *Chem. Rev.*, 2012, **112**, 1710–1717.
3 Y. X. Yan, H. Yang, X. X. Zhao, R. S. Li and X. X. Wang, Enhanced photocatalytic activity of surface disorder-engineered $CaTiO_3$, *Mater. Res. Bull.*, 2018, **105**, 286–290.
4 X. Chen and S. S. Mao, Titanium Dioxide Nanomaterials: Synthesis, Properties, Modifications and Applications, *Chem. Rev.*, 2007, **107**, 2891–2959.
5 Z. M. He, Y. M. Xia, B. Tang and J. B. Su, Fabrication and photocatalytic property of magnetic $NiFe_2O_4/Cu_2O$ composites, *Mater. Res. Express*, 2017, **4**, 095501.
6 D. Chatterjee and S. Dasgupta, Visible light induced photocatalytic degradation of organic pollutants, *J. Photochem. Photobiol. C*, 2005, **6**, 186–205.
7 L. J. Di, H. Yang, T. Xian and X. J. Chen, Enhanced photocatalytic activity of $NaBH_4$ reduced $BiFeO_3$ nanoparticles for rhodamine B decolorization, *Materials*, 2017, **10**, 1118.
8 M. Mousavi and A. H. Yangjeh, Magnetically separable ternary g-C_3N_4/Fe_3O_4/BiOI nanocomposites: novel visible-light-driven photocatalysts based on graphitic carbon nitride, *J. Colloid Interface Sci.*, 2016, **465**, 83–92.
9 A. Akhundia and A. H. Yangjeh, Facile preparation of novel quaternary g-C_3N_4/Fe_3O_4/AgI/Bi_2S_3 nanocomposites: magnetically separable visible-light-drivenphotocatalysts with significantly enhanced activity, *RSC Adv.*, 2016, **6**, 106572–106583.
10 L. J. Di, H. Yang, T. Xian and X. J. Chen, Facile synthesis and enhanced visible-light photocatalytic activity of novel p-Ag_3PO_4/n-$BiFeO_3$ heterojunction composites for dye degradation, *Nanoscale Res. Lett.*, 2018, **13**, 257.
11 J. Li, Y. Yu and L. Z. Zhang, Bismuth oxyhalide nanomaterials: layered structures meet photocatalysis, *Nanoscale*, 2014, **6**, 8473–8488.

12 P. D. Tran, L. H. Wong, J. Barber and J. S. C. Loo, Recent advances in hybrid photocatalysts for solar fuel production, *Energy Environ. Sci.*, 2012, **5**, 5902–5918.

13 J. Shang, W. C. Hao, X. J. Lv, T. M. Wang, X. LWang, Y. Du, S. X. Dou, T. F. Xie, D. J. Wang and J. O. Wang, Bismuth oxybromide with reasonable photocatalytic reduction activity under visible light, *ACS Catal*, 2014, **4**, 954–961.

14 Z. S. Liu, Z. L. Liu, J. L. Liu, J. W. Zhang, T. F. Zhou and X. Ji, Enhanced photocatalytic performance of Er-doped $Bi_{24}O_{31}Br_{10}$: Facile synthesis and photocatalytic mechanism, *Mater. Res. Bull.*, 2016, **76**, 256–263.

15 J. W. Zhang, G. Cao, H. Y. Wang, P. Z. Feng and Z. S. Liu, Graphene-$Bi_{24}O_{31}Br_{10}$ composites with tunable architectures for enhanced photocatalytic activity and mechanism, *Ceram. Int.*, 2016, **42**, 11796–11804.

16 D. N. Bui, J. Mu, L. Wang, S. Z. Kang and X. Q. Li, Preparation of Cu-loaded $SrTiO_3$ nanoparticles and their photocatalytic activity for hydrogen evolution from methanol aqueous solution, *Appl. Surf. Sci.*, 2013, **274**, 328–333.

17 X. Xiao, R. P. Hu, C. Liu, C. L. Xing, X. X. Zuo, J. M. Nan and L. S. Wang, Facile microwave synthesis of novel hierarchical $Bi_{24}O_{31}Br_{10}$ nanoflakes with excellent visible light photocatalytic performance for the degradation of tetracycline hydrochloride, *Chem. Eng. J.*, 2013, **225**, 790–797.

18 C. X. Zheng, H. Yang, Z. M. Cui, H. M. Zhang and X. X. Wang, A novel $Bi_4Ti_3O_{12}/Ag_3PO_4$ heterojunction photocatalyst with enhanced photocatalytic performance, *Nanoscale Res. Lett.*, 2017, **12**, 608.

19 Y. Peng, P. P. Yu, Q. G. Chen, H. Y. Zhou and A. W. Xu, Facile fabrication of $Bi_{12}O_{17}Br_2/Bi_{24}O_{31}Br_{10}$ type II heterostructures with high visible photocatalytic activity, *J. Phys. Chem. C*, 2015, **119**, 13032–13040.

20 X. Lou, J. Shang, L. Wang, H. F. Feng, W. C. Hao, T. M. Wang and Y. Du, Enhanced photocatalytic activity of $Bi_{24}O_{31}Br_{10}$: constructing heterojunction with BiOI, *J. Mater. Sci. Technol.*, 2017, **33**, 281–284.

21 F. T. Li, Q. Wang, J. Ran, Y. J. Hao, X. J. Wang, D. Zhao and S. Z. Qiao, Ionic liquids self-combustion synthesis of BiOBr/$Bi_{24}O_{31}Br_{10}$ heterojunctions with exceptional visible-light photocatalytic performances, *Nanoscale*, 2015, **7**, 1116–1126.

22 Y. X. Yan, H. Yang, X. X. Zhao, H. M. Zhang and J. L. Jiang, A hydrothermal route to the synthesis of $CaTiO_3$ nanocuboids using P25 as the titanium source, *J. Electron. Mater.*, 2018, **47**, 3045–3050.

23 Y. M. Xia, Z. M. He, J. B. Su, Y. Liu, B. Tang and X. P. Li, Fabrication of novel n-$SrTiO_3$/p-BiOI heterojunction for degradation of crystal violet under simulated solar light irradiation, *NANO: Brief Reports and Reviews*, 2018, **13**, 1850070.

24 J. Song, L. Zhang, J. Yang, X. H. Huang and J. S. Hu, Hierarchical porous $Bi_{24}O_{31}Br_{10}$ microarchitectures assembled by ultrathin nanosheets with strong adsorption and excellent photocatalytic performances, *Mater. Des.*, 2017, **123**, 128–136.

25 Y. Zhang, Z. R. Tang, X. Fu and Y. J. Xu, Nanocomposite of Ag-AgBr-TiO_2 as a photoactive and durable catalyst for degradation of volatile organic compounds in the gas phase, *Appl. Catal. B*, 2011, **106**, 445–452.

26 H. Guo, C. G. Niu, X. J. Wen, L. Zhang, C. Liang, X. G. Zhang, D. L. Guan, N. Tang and G. M. Zeng, Construction of highly efficient and stable ternary AgBr/Ag/$PbBiO_2Br$ *Z*-scheme photocatalyst under visible light irradiation: Performance and mechanism insight, *J. Colloid Interface Sci.*, 2018, **513**, 852–865.

27 X. X. Zhao, H. Yang, S. H. Li, Z. M. Cui and C. R. Zhang, Synthesis and theoretical study of large-sized $Bi_4Ti_3O_{12}$ square nanosheets with high photocatalytic activity, *Mater. Res. Bull.*, 2018, **107**, 180–188.

28 S. J. Zhang and J. F. Yang, Microwave-assisted synthesis of BiOCl/BiOBr composites with improved visible-light photocatalytic activity, *Ind. Eng. Chem. Res.*, 2015, **54**, 9913–9999.

29 H. B. Yin, X. F. Chen, R. J. Hou, H. J. Zhu, S. Q. Li, Y. N. Huo and H. X. Li, Ag/BiOBr film in a rotating-disk reactor containing long-afterglow phosphor for round-the-clock photocatalysis, *ACS Appl. Mater. Interfaces*, 2015, **7**, 20076–20082.

30 C. H. Cao, L. Xiao, C. H. Chen and Q. H. Cao, Synthesis of novel Cu_2O/BiOCl heterojunction nanocomposites and their enhanced photocatalytic activity under visible light, *Appl. Surf. Sci.*, 2015, **357**, 1171–1179.

31 Y. M. Xia, Z. M. He, Y. L. Lu, B. Tang, S. P. Sun, J. B. Su and X. P. Li, Fabrication and photocatalytic property of magnetic $SrTiO_3/NiFe_2O_4$ heterojunction nanocomposites, *RSC Adv.*, 2018, **8**, 5441–5450.

32 Y. M. Xia, Z. M. He, K. J. Hu, B. Tang, J. B. Su, Y. Liu and X. P. Li, Fabrication of n-$SrTiO_3$/p-Cu_2O heterojunction composites with enhanced photocatalytic performance, *J. Alloys Compd.*, 2018, **753**, 356–363.

33 X. Xiao, R. P. Hu, C. Liu, C. L. Xing, X. X. Zuo, J. M. Nan and L. S. Wang, Facile microwave synthesis of novel hierarchical $Bi_{24}O_{31}Br_{10}$ nanoflakes with excellent visible light photocatalytic performance for the degradation of tetracycline hydrochloride, *Chem. Eng. J.*, 2013, **225**, 790–797.

34 J. Shang, W. C. Hao, X. J. Lv, T. MWang, X. LWang, Y. Du, S. X. Dou, T. F. Xie, D. J. Wang and J. O. Wang, Bismuth oxybromide with reasonable photocatalytic reduction activity under visible light, *ACS Catal*, 2014, **4**, 954–961.

35 Y. F. Lin and Y. J. Hsu, Interfacial charge carrier dynamics of type-II semiconductor Nanoheterostructures, *Appl. Catal., B*, 2013, **130–131**, 93–98.

36 Ye, H. Yang, H. M. Zhang and J. L. Jiang, A promising $Ag_2CrO_4/LaFeO_3$ heterojunction photocatalyst applied to photo-Fenton degradation of RhB, *Environ. Technol.*, DOI: 10.1080/09593330.2018.1538261.

37 I. K. Konstantinou and T. A. Albanis, TiO_2-assisted photocatalytic degradation of azo dyes in aqueous solution: kinetic and mechanistic investigations: a review, *Appl. Catal., B*, 2004, **49**, 1–14.

38 C. X. Zheng and H. Yang, Assembly of Ag_3PO_4 nanoparticles on rose flower-like Bi_2WO_6 hierarchical architectures for achieving high photocatalytic performance, *J. Mater. Sci.: Mater. Electron.*, 2018, **29**, 9291–9300.

39 Y. M. Xia, Z. M. He, J. B. Su, B. Tang, K. J. Hu, Y. L. Lu, S. P. Sun and X. P. Li, Fabrication of magnetically separable $NiFe_2O_4$/BiOI nanocomposites with enhanced photocatalytic performance under visible-light irradiation, *RSC Adv.*, 2018, **8**, 4284–4294.

40 Zhao, H. Yang, Z. Cui and W. F. R Li, Enhanced photocatalytic performance of Ag-$Bi_4Ti_3O_{12}$ nanocomposites prepared by a photocatalytic reduction method, *Mater. Technol.*, 2017, **32**, 870–880.

41 Y. M. Xia, Z. M. He, W. Yang, B. Tang, Y. L. Lu, K. J. Hu, J. B. Su and X. P. Li, Effective charge separation in BiOI/Cu_2O composites with enhanced photocatalytic activity, *Mater. Res. Express*, 2018, **5**, 025504.

42 S. M. Wang, D. L. Li, C. Sun, S. G. Yang, Y. Guan and H. He, Highly efficient photocatalytic treatment of dye wastewater via visible-light-driven AgBr-Ag_3PO_4/MWCNTs, *J. Mol. Catal. A: Chem.*, 2014, **383–384**, 128–136.

43 Z. M. He, B. Tang, J. B. Su and Y. M. Xia, Fabrication of novel $Cu_2O/Bi_{24}O_{31}Br_{10}$ composites and excellent photocatalytic performance, *J. Mater. Sci.: Mater. Electron.*, 2018, **29**, 19544–19553.

44 Z. M. He, Y. M. Xia, B. Tang, X. F. Jiang and J. B. Su, Fabrication and photocatalytic property of ZnO/Cu_2O core-shell nanocomposites, *Mater. Lett.*, 2016, **184**, 148–151.

45 Tachikawa, M. Fujitsuka and T. Majima, Mechanistic insight into the TiO_2 photocatalytic reactions: Design of new photocatalysts, *J. Phys. Chem. C.*, 2007, **111**, 5259–5275.

46 Y. C. Pu, W. H. Lin and Y. J. Hsu, Modulation of charge carrier dynamics of $Na_xH_{2-x}Ti_3O_7$-Au-Cu_2O *Z*-scheme nanoheterostructures through size effect, *Appl. Catal., B*, 2015, **163**, 343–351.

47 Y. H. Chiu and Y. J. Hsu, Au@Cu_7S_4 yolk @ shell nanocrystal-decorated TiO_2 nanowires as an all-day active photocatalyst for environmental purification, *Nano Energy*, 2017, **31**, 286–295.

48 Xia, Z. M. He, J. B. Su, B. Tang and Y. Liu, Enhanced photocatalytic performance of *Z*-scheme Cu_2O/Bi_5O_7I nanocomposites, *J. Mater. Sci.: Mater. Electron.*, 201, **29**, 15271–15281.

49 J. M. Li, H. Y. Cheng, Y. H. Chiu and Y. J. Hsu, ZnO-Au-SnO_2 Z-scheme photoanodes for remarkable photoelectrochemical water splitting, *Nanoscale*, 2016, **8**, 15720.

50 X. Xiao, C. X. Zheng, M. L. Lu, L. Zhang, F. Liu, X. X. Zuo and J. M. Nan, Deficient $Bi_{24}O_{31}Br_{10}$ as a highly efficient photocatalyst for selective oxidation of benzyl alcohol into benzaldehyde under blue LED irradiation, *Appl. Catal., B*, 2018, **228**, 142–151.

51 Y. C. Ye, H. Yang, X. X. Wang and W. J. Feng, Photocatalytic, Fenton and photo-Fenton degradation of RhB over Z-scheme g-C_3N_4/$LaFeO_3$ heterojunction photocatalysts, *Mater. Sci. Semicond. Process.*, 2018, **82**, 14–24.

52 Y. M. Xia, Z. M. He, B. Tang, J. B. Su and Y. Liu, Enhanced photocatalytic performance of Z-scheme Cu_2O/Bi_5O_7I nanocomposites, *J. Mater. Sci.: Mater. Electron.*, 2018, **29**, 15271–15281.